The Dominant Patterns of Intraseasonal Rainfall Variability in May–October and November–April over the Tropical Western Pacific🖉

SUNIL KUMAR PARIYAR, NOEL KEENLYSIDE, BHUWAN CHANDRA BHATT, AND
NOUR-EDDINE OMRANI

Geophysical Institute and Bjerknes Centre for Climate Research, University of Bergen, Bergen, Norway

ABSTRACT

The space–time structure of intraseasonal (10–90 day) rainfall variability in the western tropical Pacific is studied using daily 3B42 TRMM and ERA-Interim reanalysis data for the period 1998–2014. Empirical orthogonal function (EOF) analysis of 10–90-day filtered daily rainfall anomalies identifies two leading modes in both May–October and November–April; together these modes explain about 11%–12% of the total intraseasonal variance over the domain in both seasons and up to 60% over large areas of the western Pacific in both climatological periods. The two leading modes in May–October are linearly related to each other and both are well correlated with the Madden–Julian oscillation (MJO) indices. Although the two leading EOF modes in November–April are linearly independent of each other, both show statistically significant correlations with the MJO. The phase composites of 30–80-day filtered data show that the two leading modes are associated with strong eastward and northward propagation of rainfall anomalies in May–October, and eastward and southward propagation of rainfall anomalies in November–April. The eastward propagation of rainfall anomalies in both seasons and southeastward propagation related with EOF2 in November–April is linked to the development of low-level moisture flux convergence ahead of the active convection. Similarly, the northward propagation in May–October is also connected with low-level moisture flux convergence, but surface wind and evaporation variations are also important. The wind–evaporation–SST feedback mechanism drives the southeastward propagation of rainfall anomalies associated with EOF1 in November–April. The different mechanisms for southeastward propagation associated with two leading modes in November–April suggest dynamically different relations with the MJO.

1. Introduction

The rainfall variability in the tropical western Pacific is characterized by the intertropical convergence zone (ITCZ) in the Northern Hemisphere (Bain et al. 2011), and the South Pacific convergence zone (SPCZ) in the Southern Hemisphere (Haffke and Magnusdottir 2013). The rainfall variability in this region is largely controlled by the dynamics of these large-scale rainfall bands and their interactions with the El Niño–Southern Oscillation (ENSO) and the Madden–Julian oscillation (MJO) at different time scales (Lau et al. 1989; Folland et al. 2002; McPhaden et al. 2006; Hendon et al. 2007; Matthews 2012; Haffke and Magnusdottir 2013; Zhang 2013;

Borlace et al. 2014). In particular, the intraseasonal oscillation is one of the most significant signals over the tropical Indian Ocean, the Maritime Continent, and the tropical western Pacific (Zhang 2005, 2013).

The intraseasonal time scale dominates rainfall variability in the western Pacific and it has a great impact on the livelihood of people inhabiting the Pacific Island countries. Figures 1a and 1b show the explained variance of the intraseasonal rainfall variability (10–90-day band) to the total daily variance over the western Pacific for May–October and November–April based on daily Tropical Rainfall Measuring Mission (TRMM) 3B42 data from 1998 to 2014. In particular, up to 60% of the daily rainfall variance is observed within the intraseasonal time scale (Figs. 1a,b). The intraseasonal rainfall variability is essential for the Pacific island countries where the domestic and agricultural water demands highly depend upon the regular rainfall, because of limited water management infrastructure (Falkland and Custodio 1991; White et al. 1999; Falkland 2002; Gawander 2007). Thus,

---

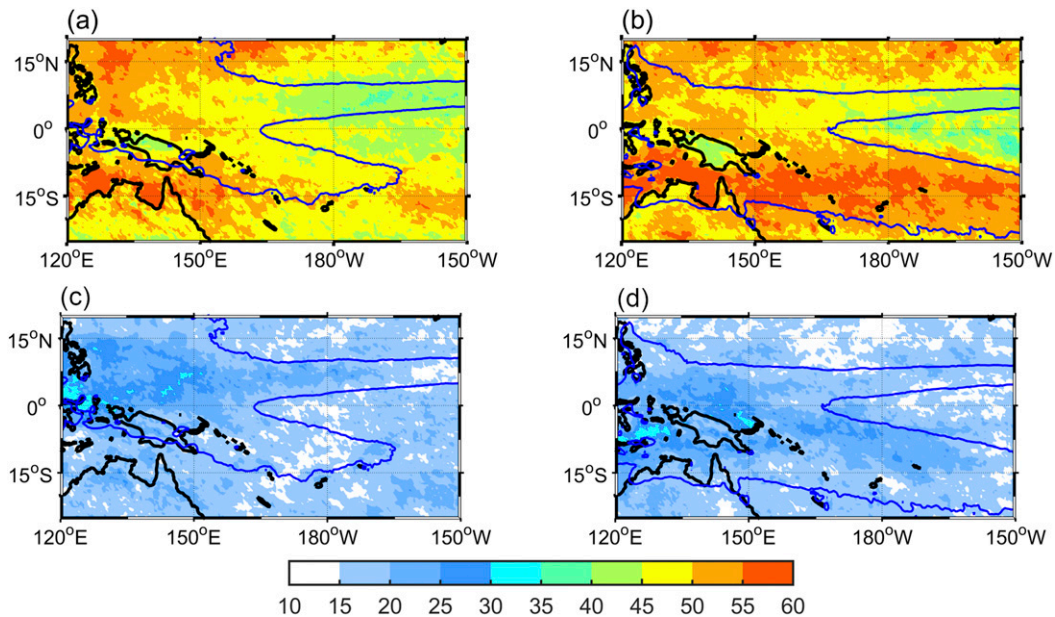*Corresponding author*: Sunil Kumar Pariyar, sunil.pariyar@uib.no

FIG. 1. Fraction of daily intraseasonal (10–90 day) rainfall variance (%) to the total daily variance in (a) May–October and (b) November–April. Fraction of daily intraseasonal (10–90 day) variance (%) explained by the MJO in (c) May–October and (d) November–April. The 5-mm daily rainfall climatology from 1998 to 2014 is represented by blue contours.

understanding intraseasonal rainfall variability is useful for improving the prediction of rainfall on these time scales for this region; and improvement in rainfall prediction skill on these time scales could be useful in agricultural decision making, like on the timing of planting and harvesting, use of fertilizers, and the need for irrigation.

The MJO is the primary source of intraseasonal variability in the tropical Indo-Pacific region (Madden and Julian 1994; Zhang 2005, 2013). It is characterized by large-scale deep convective rainfall anomalies, originating from the Indian Ocean, propagating to the east through the Maritime Continent and into the western Pacific (Knutson and Weickmann 1987; Rui and Wang 1990; Hendon and Salby 1994; Matthews 2000; Zhang 2005; Hsu and Lee 2005, DeMott et al. 2015; Tseng et al. 2017). The fraction of daily intraseasonal rainfall variance associated with the MJO compared to the total 10–90-day rainfall variance is presented in Figs. 1c and 1d. The MJO explains up to 35% of the intraseasonal variance over the western North Pacific in May–October (Fig. 1c), and up to 25% over the South Pacific in November–April (Fig. 1d). As the MJO explains a considerable amount of the total daily rainfall variance in the 10–90-day band, it is important to understand the impacts of the MJO on the intraseasonal rainfall variability over the western Pacific and the possible mechanisms involved in MJO–western Pacific rainfall teleconnection.

Past studies on the intraseasonal rainfall variability in this region focused mostly on the western North Pacific (Murakami 1980; Lau and Chan 1986; Chen and Murakami 1988; Lau et al. 1988; Tanaka 1992; Ding 1992; Nakazawa 1992; Wang and Xu 1997; Kang et al. 1999; Chen et al. 2000; Wu and Wang 2001; Li and Wang 2005; Wang et al. 2009) and very few studies discussed the intraseasonal rainfall variability and its propagation in the South Pacific (e.g., Matthews and Li 2005; Matthews 2012; Van Der Wiel et al. 2015). Proposed mechanisms for eastward propagation of the MJO include wind–evaporation–SST feedback or wind-induced surface heat exchange (Emanuel 1987; Neelin et al. 1987; Xie and Carton 2004; Lin et al. 2008), wave–CISK (conditional instability of the second kind) (Lau and Peng 1987; Yamasaki 1969; Lindzen 1974), frictional wave–CISK (Wang 1988; Wang and Rui 1990; Xie and Kubokawa 1990), convection–water vapor feedback and self-regulating moisture modes (Bladé and Hartmann 1993; Kemball-Cook and Weare 2001; Bretherton et al. 2005; Raymond and Fuchs 2009), and multiscale interactions (Majda and Klein 2003; Majda and Biello 2004; Biello and Majda 2005; Majda and Stechmann 2009). The relevance of these mechanisms for driving intraseasonal rainfall variability over the western Pacific has not been fully studied and it is not clear which of the proposed mechanism is more appropriate for this region. In this context, the present study investigates the dominant large-scale intraseasonal (10–90 day) rainfall

patterns over the western Pacific, its characteristics, its connection with the MJO, and possible mechanisms by using the daily TRMM rainfall and ERA-Interim reanalysis data from 1998 to 2014. Specifically, this work addresses the following questions: (i) What are the dominant intraseasonal rainfall patterns in the tropical western Pacific in May–October and November–April? (ii) What is the role of the MJO on the dominant intraseasonal rainfall modes in this region? (iii) What are the fundamental mechanisms involved in the intraseasonal rainfall variability?

2. Data and methods

The analysis of 10–90-day rainfall variability uses both observed and reanalysis datasets. The observed daily TRMM-3B42 version 7 rainfall estimates (Huffman et al. 2007) are used for EOF analysis. The TRMM data between 1998 and 2014 with a horizontal resolution of 0.25° is used. The reanalysis data is used to understand the atmospheric dynamics associated with the observed rainfall patterns. The daily ERA-Interim reanalysis at 0.75° × 0.75° horizontal resolution over the same period is used (Dee et al. 2011). The selected surface variables are sea level pressure (SLP), sea surface temperature (SST), 10-m zonal and meridional wind speed (WS), evaporation (EVP), and vertically integrated moisture flux divergence (VIMFD). Similarly, the pressure level fields are specific humidity (SH), and zonal and meridional winds. The daily total evaporation is computed by summing the cumulative evaporation of two 12-h forecasts initiated at 0000 and 1200 UTC. The daily values for all other variables are computed by averaging over four 6-hourly values. The velocity potential (VP) at 200 hPa is computed from the daily zonal and meridional winds. The MJO is defined by using the all season Real-time Multivariate MJO (RMM) index suggested by Wheeler and Hendon (2004). The daily RMM index data are obtained from the Australian Bureau of Meteorology website (http://www.bom.gov.au/climate/mjo/). The RMM index consists of the first two leading PCs (RMM1 and RMM2) obtained from the combined EOF analysis of daily outgoing longwave radiation, 850-hPa zonal wind, and 200-hPa zonal wind averaged over 15°S–15°N.

From the daily rainfall and atmospheric data, daily anomalies are computed by subtracting the smoothed multiyear mean annual cycle (sum of the first four harmonics decomposed from the mean annual cycle). The anomalies are then detrended to remove the long-term trend. To retain the intraseasonal variability only, we filter out the daily detrended anomalies by applying 10–90-day bandpass Butterworth filter. Principal component analysis (PCA) also known as empirical orthogonal function

(EOF) analysis is used to understand the dominant large-scale rainfall patterns over the western Pacific. The EOF analysis is performed for daily 10–90-day filtered TRMM rainfall anomalies in May–October and November–April separately.

To test the significance of the leading EOF modes, we implemented the Dommenget (2007) stochastic null hypothesis test that compares the observed EOF modes with the EOF modes of the fitted null hypothesis. The null hypothesis is that the data can be explained by a first-order autoregressive process, which is fitted to the statistics of the observed time series. The observed EOF modes that are statistically different from the fitted EOF modes are called distinct EOF modes (DEOFs). The DEOF modes are assumed to differ from the stochastic noise hypothesis because of a differing physical mechanism. Along with the null hypothesis test, we also apply North's rule to confirm whether the selected modes are statistically distinguishable from each other and from other higher modes (North et al. 1982).

The power spectra of daily PC time series are computed by averaging the individual power spectrum for each of the 17 (16) years in May–October (November–April). To test the statistical significance of power spectra, the mean spectrum is compared with a red-noise spectrum and associated 99.9% confidence level (Torrence and Compo 1998). The 99.9% confidence level is obtained by multiplying the red noise spectrum by the 99.9th percentile value of the chi-squared distribution (Gilman et al. 1963). To determine the confidence level, 34 (17 years in total for May–October) and 32 degrees of freedom (16 years in total for November–April) are used by assuming roughly 2 degrees of freedom for each seasonal spectral estimate (Feldstein 2000). Lag correlation analysis between the principal components (PCs) is done to identify the phase relation between leading variability patterns. Likewise, we perform lag correlation analysis to establish a relationship between the MJO and the leading rainfall variability patterns. For the statistical significance of lag correlation coefficients, the two-tailed Student's t statistic is used. Because, the characteristic time scale of intraseasonal variability is on the order of 30–80 days, the degrees of freedom for the t statistic is estimated by identifying the number of independent intraseasonal cycles of 30–80-day time scale. For each season with an approximate length of 180 days, four to six cycles are observed in each PC. Taking five cycles per season results in roughly 75 cycles in total. Hence, for 73 ($n - 2$) degrees of freedom, the critical value of Pearson's correlation coefficient at 95% level is 0.2. The observed correlation coefficients above this value are considered as statistically significant.

To quantify the impact of the MJO on the 30–80-day rainfall variability over the western Pacific, multiple regression analysis is performed between daily 30–80-day
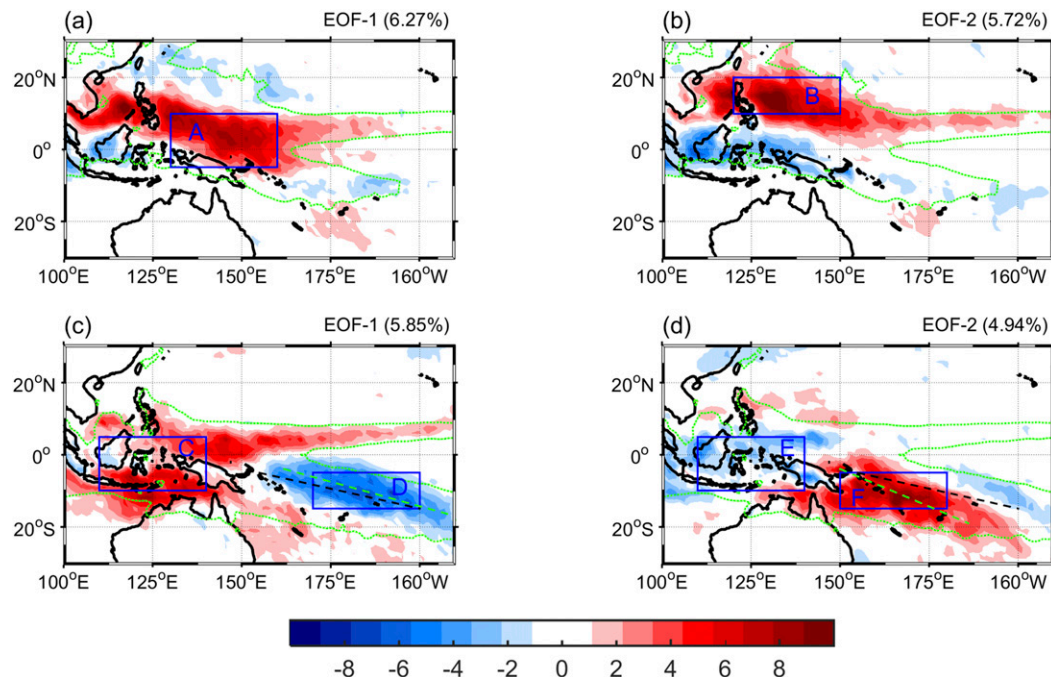
FIG. 2. Spatial structures of leading EOF modes of rainfall (mm day^{-1}) based on daily 10–90-day bandpass-filtered data in (a),(b) May–October and (c),(d) November–April. The two leading modes in May–October and November–April explain about 12% and 11% of the total intraseasonal variance. The 5-mm daily seasonal climatological rainfall is represented by the green contours. Black dashed diagonal lines are the climatological position of the mean rainfall axis of the SPCZ. The green dashed diagonal lines are the diagonal axes considered for computing time–latitude plots for November–April in section 4c(3). The blue boxes (A–F) indicate the region chosen to compute area-averaged rainfall and other atmospheric variables for the explanation of the mechanism in section 4c(3).

filtered rainfall anomalies and RMM indices. Composites of rainfall anomalies at different lags are computed by selecting strong events based on standardized PCs in order to understand the space–time evolution of each EOF mode. The statistical significance of the composites is assessed by implementing two-tailed Student's t test at 95% confidence level (Harrison and Larkin 1998). To understand the general atmospheric condition associated with each EOF pattern, anomaly composites of different atmospheric fields at zero lag are constructed, and this is followed by a significance test similar to that of the rainfall anomaly composites. Furthermore, the space–time evolution of leading EOF modes and the associated mechanisms are studied by lag composites of rainfall and other atmospheric-variable anomalies. These are computed over six selected regions of maximum rainfall variance, as identified from the EOF modes.

3. Dominant patterns of intraseasonal (10–90 day) rainfall variability

The temporal and spatial characteristics of leading patterns of western Pacific intraseasonal rainfall variability are identified by EOF analysis of 10–90-day

bandpass-filtered daily rainfall anomalies from 25°S–20°N to 120°E–150°W; May–October and November–April seasons are analyzed separately. The sensitivity of the EOF analysis to the domain was checked by repeating the analysis for various domains covering the western Pacific. The EOF modes for different domain sizes show high positive pattern correlation coefficients that are statistically significant at the 95% level. This suggests that the leading EOF modes are not sensitive to the selected domain size. The first two EOF modes in both seasons are significantly different from variability generated by stochastic isotropic diffusion (Dommenget 2007). According to North's rule, the first two modes in both seasons are also well separated from higher modes.

Figure 2 shows the spatial structure of the leading EOF modes for May–October and November–April. The first two EOF modes explain about 11%–12% of total 10–90-day rainfall variance in both May–October and November–April. Though the total explained variances are not very high, the first two modes explain about 40% to 60% of the total daily rainfall variance in some larger areas (Fig. S1 in the online supplemental material) that have relatively higher climatological rainfall and relatively large intraseasonal variance, such
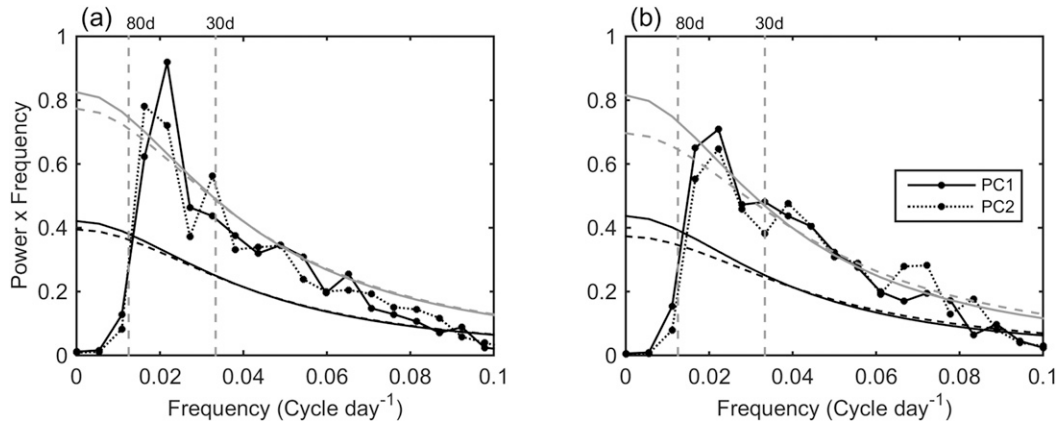
FIG. 3. Power spectra of each PC of the first two leading EOF modes in (a) May–October and (b) November–April. The power spectrum is calculated separately for each year with 184 and 181 sample size for May–October and November–April and then averaged over the respective 17 and 16 seasons from 1998 to 2014. The solid black line with the circle is for PC1 and the dotted line with the circle is for PC2. The red noise spectrum represented by two lower black lines without circle (PC1: solid; PC2: dashed) is computed from lag-one autocorrelation. The upper two gray lines without circle (PC1: solid; PC2: dashed) is the 99.9% confidence level needed to reject a null hypothesis of red noise.

as western North Pacific in May–October and SPCZ in November–April (Figs. 1a,b). In May–October, the EOF1 mode shows large-scale rainfall anomalies of one sign over the western North Pacific (Fig. 2a), and the EOF2 mode shows a meridional dipole structure with a variance maximum located at 15°N and another located over the Maritime Continent (Fig. 2b). On the other hand, the first two EOF modes in the November–April have maximum loadings over the South Pacific. The EOF1 mode in November–April has a maximum in rainfall variance that is collocated with the observed climatological position of the SPCZ (dashed black diagonal line in Fig. 2c); we will term this mode the suppressed-enhanced SPCZ mode. In contrast, the EOF2 mode has its maximum variance southwest of the mean SPCZ position and we will refer to it as the shifted SPCZ mode. The mean position of the SPCZ (black dashed lines in Figs. 2c,d) is constructed by following the maximum rainfall along the SPCZ of daily rainfall climatology (1998–2014).

The power spectra of the PCs show dominant peaks between 30–80-day period in both seasons (Fig. 3). In May–October, these dominant spectral peaks are significantly different from the null hypothesis of a stochastic auto-regressive process of order one, while in November–April the variability is more consistent with the null hypothesis. The fraction of total intraseasonal daily rainfall variance concentrated in the 30–80-day band is approximately 49% for both PCs in May–October, while in November–April the fractions are 47% and 41% for PC1 and PC2, respectively. The power spectra in the 10–30-day band in both seasons for both PCs do not provide strong evidence for a preferred oscillatory time scale, although the spectral peaks

at roughly 25 and 15 days for the EOF2 mode in November–April are statistically significant. In this study, we will only focus on the 30–80-day band because it contains a large part of the variance, there are distinct spectral peaks, and it coincides with the typical time scale of the MJO (Wheeler and Hendon 2004); we leave the analysis of the higher-frequency (10–30 day) part of the variability for future work.

To investigate the phase relationship between PCs, we computed the lag correlation between PC1 and PC2 (Fig. 4). The lag correlation is performed for the raw PCs (solid line) and the 30–80-day bandpass-filtered PCs (dashed line); here it is more meaningful to compute the correlation coefficients from 30–80-day bandpass-filtered data because we will focus mostly on this time scale. In May–October, PC1 tends to lead PC2 by about six (eight) days with a maximum correlation of 0.44 (0.56) for unfiltered (filtered) data (Fig. 4a). While the relationship between PCs is not asymmetric with respect to the positive and negative phases for the unfiltered data, they are nearly asymmetric for filtered data. This suggests that the two EOF modes in May–October represent different phases of the same mode of variability. In contrast, the two PCs in November–April show a very weak correlation of 0.23 for the filtered time series, and no significant correlation for the unfiltered data (Fig. 4b). Thus, the two EOF modes in November–April are treated as two different modes.

4. Low-frequency (30–80 day) intraseasonal variability

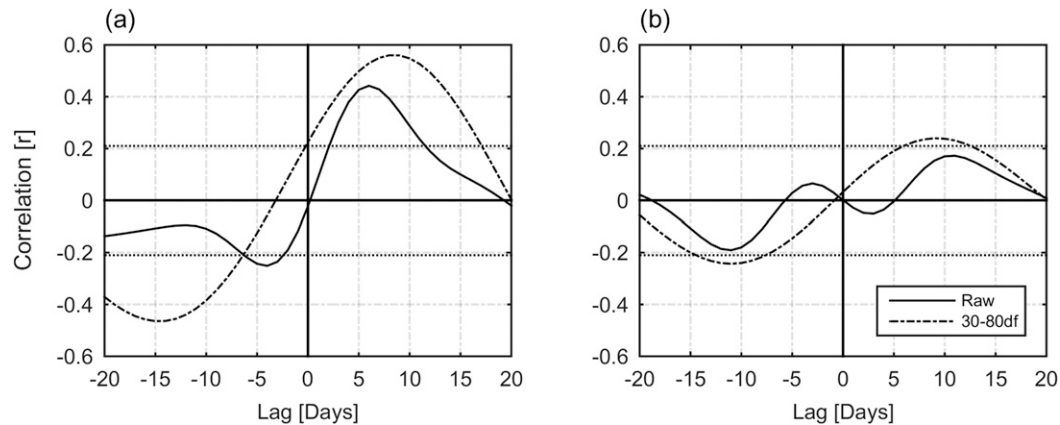We now focus on the 30–80-day frequency band in order to understand the mechanisms driving the

FIG. 4. Lag correlation between daily time series of PC1 and PC2 in (a) May–October and (b) November–April. The correlation is computed for each year with 184 and 181 days segments for May–October and November–April and then averaged over respective 17 and 16 seasons from 1998 to 2014. The solid line is for raw PCs (10–90 day) and the dashed lines are for PCs after applying 30–80-day bandpass filter. Positive (negative) values indicate lead (lag). Positive lags are PC1 leading PC2. The horizontal dotted line represents the 95% confidence level based on two-tailed Student's t test.

enhanced rainfall variability on these time scales, particularly during May–October, and its relation to the MJO. The results presented in this section are based on the 30–80-day bandpass-filtered data unless stated otherwise. To understand the space–time structures, lag composites of rainfall anomalies are computed after applying a 30–80-day bandpass filter to both daily PCs and rainfall anomalies. Furthermore, we consider only PC1 for May–October, and both PCs for November–April; for May–October we do not consider PC2 because of its relatively strong lag relation to PC1. Positive events are identified by local maximum PC values that are greater than 0.5 standard deviations; negative events are similarly defined. Lag composites are computed by averaging rainfall anomalies over all events for each day from the 16 days before to 16 days after the peak event (i.e., a centered 33-day segment).

a. Space–time structures

In general, the two leading patterns of 30–80-day rainfall variability over the western Pacific in May–October and November–April are associated with MJO-like large-scale rainfall structures over the Indian Ocean and the western Pacific (Fig. 5). In both seasons, eastward propagation of rainfall anomalies from the Indian Ocean to the western Pacific is evident between −16 days to zero lag. Apart from eastward propagation, northward propagation in May–October and southeastward propagation in November–April are also observed.

In May–October, 16 days before the EOF1 mode peaks there is enhanced rainfall over the Indian Ocean and suppressed rainfall over the western North Pacific. As the event develops, the positive rainfall anomalies

propagate from the Indian Ocean through the Maritime Continent, reaching maximum values over the western North Pacific at zero lag (Fig. 5a). The positive rainfall anomalies also propagate northward from the equatorial western Pacific to the South China Sea. Meanwhile, the dry anomalies from the Indian Ocean replace the positive anomalies over the equatorial western Pacific, producing a north–south dipole structure at +8 days. This pattern is fairly similar to the spatial structure of the EOF2 mode (see Fig. 2b). This is consistent with the two EOF modes in May–October representing different phases of an eastward and northward propagating pattern of intraseasonal variability. At +16 days, the rainfall anomalies over the South China Sea weaken, to be replaced by northward propagating negative anomalies from the equatorial region. The northward propagation is also observed over the Indian Ocean and the Maritime Continent during the eastward propagating phase.

In November–April, both EOF modes exhibit similar eastward propagation of 30–80-day rainfall anomalies from the Indian Ocean to the Maritime Continent, but they show different propagation characteristics from the Maritime Continent to the South Pacific (Figs. 5b,c). For the EOF1 mode, the positive rainfall anomalies propagate from the Indian Ocean to the Maritime Continent from −16 days until its peak at zero lag (Fig. 5b). The propagation of rainfall anomalies from the Maritime Continent to the South Pacific is less clear, with a somewhat abrupt intensification of the SPCZ from −8 to −16 days. For the EOF2 mode, 16 days before the event's peak, rainfall is enhanced over the Maritime Continent and suppressed over the South Pacific (Fig. 5c). The positive rainfall anomalies then propagate from the
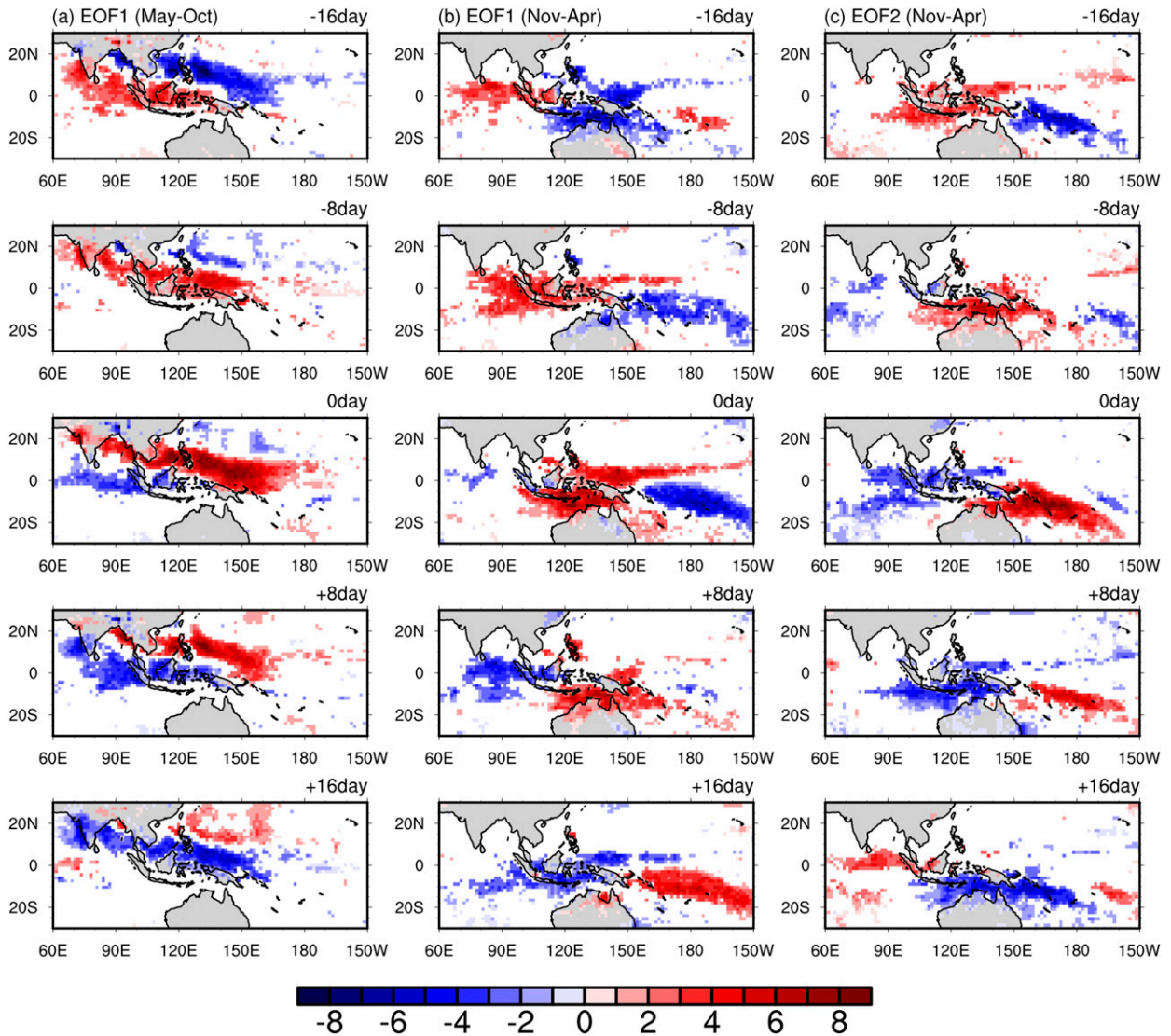
FIG. 5. Rainfall life cycle anomaly composites (mm day^{-1}) of (left) EOF1 in May–October, (middle) EOF1 in November–April, and (right) EOF2 in November–April. The composites are computed from the daily 30–80-day bandpass-filtered data. Events with an amplitude greater than 0.5 standard deviations of the normalized PCs are considered for this composition and only statistically significant values at 95% confidence level are shown.

Maritime Continent to replace the negative anomalies in the South Pacific at the event's peak. As the event decays, the positive rainfall anomalies in the South Pacific become weaker and are replaced by negative anomalies at +16 days. The propagation of rainfall anomalies from the Maritime Continent to the South Pacific is more pronounced for the EOF2 mode compared to the EOF1 mode.

b. Relation to the MJO

As presented in the previous section, the time evolution of each of the dominant patterns of 30–80-day rainfall variability over the western Pacific shows similar space–time structures to the MJO (Fig. 5). To assess the relationship between the MJO and these patterns of variability, we perform the lag correlations among daily time series of 30–80-day bandpass-filtered PCs and RMM indices (Fig. 6). The maximum lag correlations among PCs and RMM indices are higher in May–October than November–April. In May–October, RMM1 leads PC1 by 1 day with a maximum correlation of 0.71, while PC1 leads RMM2 by 8 days with a maximum correlation of 0.62 (Fig. 6a). Similarly, for PC2, RMM1 leads PC2 by 8 days with a correlation of 0.56 and the correlation between PC2 and RMM2 is maximum ($r \sim 0.65$) at lag zero (Fig. 6b). In November–April,
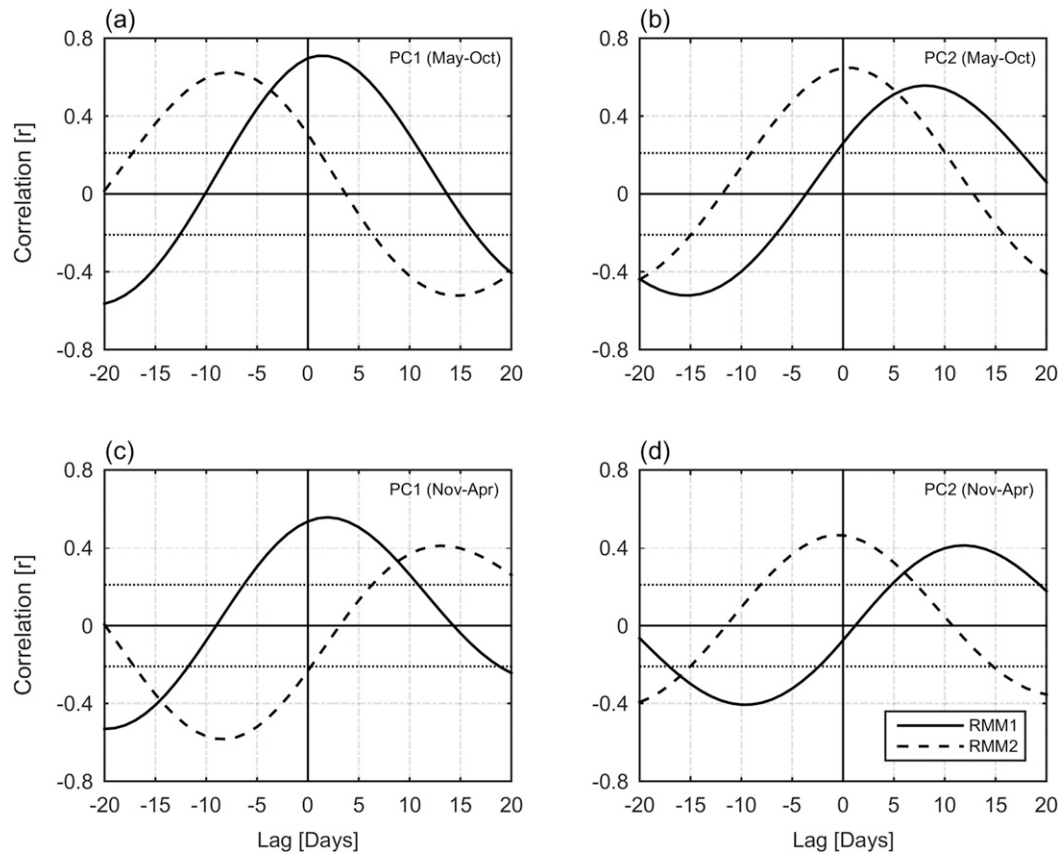
FIG. 6. Lag correlation of each PC with RMM1 (solid lines) and RMM2 (dashed lines) index in (a),(b) May–October and (c),(d) November–April for 30–80-day period. The correlation is computed for each year with 184 and 181 days segments for May–October and November–April and then averaged over respective 17 and 16 seasons from 1998 to 2014. The horizontal dotted line represents the 95% confidence level based on two-tailed Student's t test. For positive lag, the RMM indices lead the PCs.

RMM1 leads PC1 by 2 days ($r \sim 0.56$) and the negative of PC1 leads RMM2 by 8 days ($r \sim -0.58$) (Fig. 6c). For PC2, RMM1 leads PC2 by 12 days ($r \sim 0.41$) and PC2 leads RMM2 by 1 day ($r \sim 0.46$) (Fig. 6d). To quantify the variance explained by the MJO in the 30–80-day band, we construct multiple linear regression models (four in total) for each of the 30–80-day filtered PCs in both seasons using both RMM indices. In May–October, the MJO explains about 61% of the 30–80-day PC1 variance and about 53% of the PC2 variance. Similarly, in November–April, the MJO explains about 47% of the 30–80-day PC1 variance and about 37% of the PC2 variance.

To further identify which phase of the MJO is more relevant to the observed EOF patterns, we compute the pattern correlation coefficients between each of the EOF modes and the rainfall anomaly composite patterns associated with each of the eight MJO phases. In May–October, the EOF1 mode has a maximum positive pattern correlation with the MJO phase 5 rainfall composite ($r \sim 0.92$), and the EOF2 mode has a maximum

correlation with the MJO phase 6 rainfall composite ($r \sim 0.89$). While in November–April, phase 4 ($r \sim 0.76$) and 6 ($r \sim 0.65$) show maximum positive correlations with EOF1 and EOF2, respectively.

c. Dynamical explanation of 30–80-day variability

Three different types of analysis are performed to identify the physical mechanisms driving rainfall variability on the 30–80-day time scale. First, the anomaly phase composites of atmospheric variables and rainfall at zero lag are computed to understand the general atmospheric features associated with each EOF mode. Second, time–longitude and time–latitude plots of rainfall anomalies are constructed to characterize the zonal and meridional propagation of the rainfall patterns. Last, lag composites of area-averaged anomalies of rainfall and atmospheric variables are computed to illustrate the propagation mechanisms. We summarize these analyses in the subsections below. Please note the following: The climatological winds (Fig. S2) are considered in discussions of wind-driven

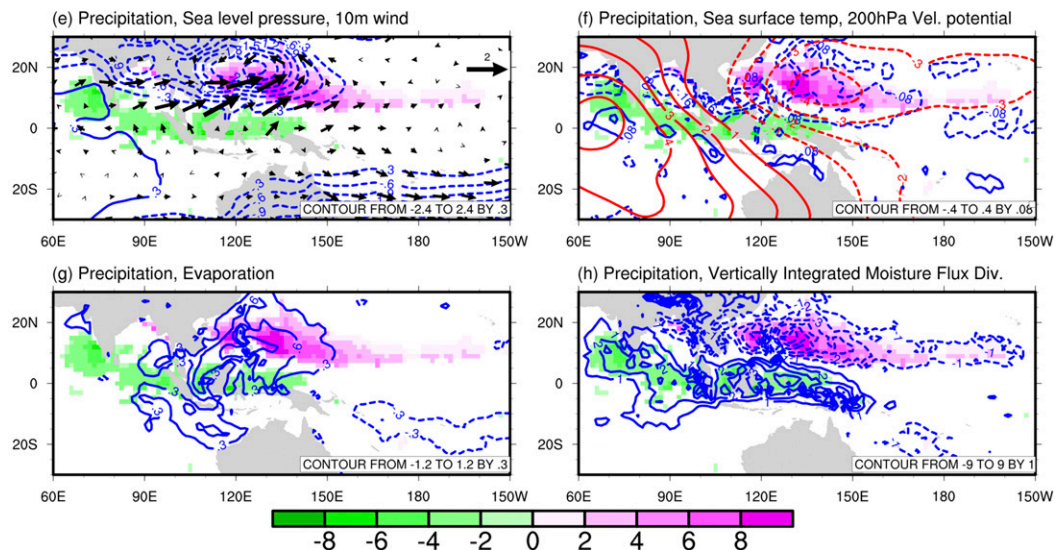## EOF1 (May–Oct)
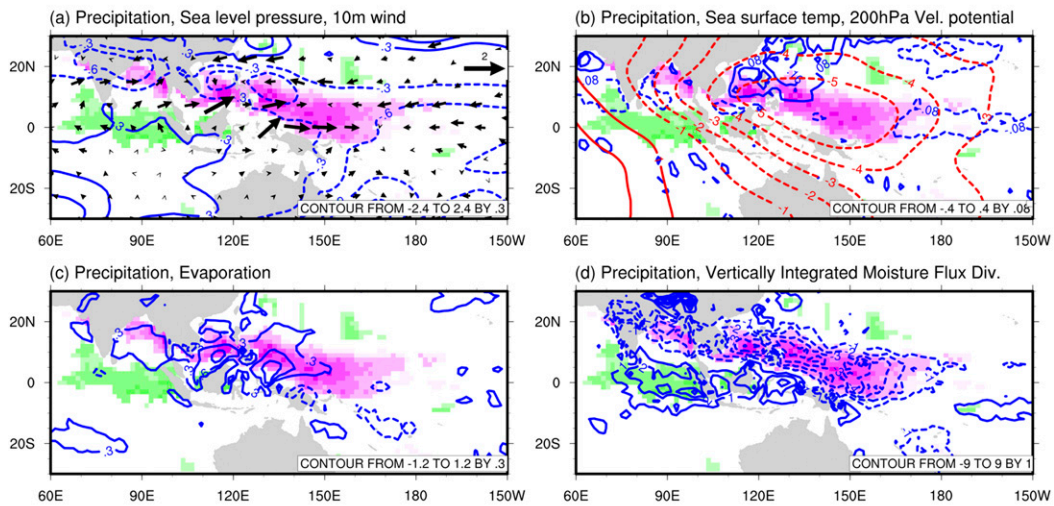
EOF2 (May–Oct)

FIG. 7. Composites of rainfall anomalies (shaded), and anomalies of atmospheric variables (contours and vectors) for 30–80-day period associated with (a)–(d) PC1 and (e)–(h) PC2 in May–October. Blue contours in (a),(e) show SLP (mb), in (b),(f) show SST (°C), in (c),(g) evaporation (mm day^{-1}), and in (d),(h) show vertically integrated moisture flux divergence (10^{-5} kg m^{-2} s^{-1}). Black vectors in (a),(e) show the 10-m wind (m s^{-1}); and red contours in (b),(f) show the 200-hPa velocity potential (10^{6} m^{2} s^{-1}). The solid contours are positive values and dashed are negative values. Only significant values at 95% confidence level are shown.

evaporation. We consider the moisture flux divergence integrated vertically over the entire air column when relating rainfall patterns to atmospheric circulation (Figs. 7 and 8), while low-level (1000 hPa) moisture flux divergence is used to represent the propagation mechanism in section 4c(3). The moisture flux divergence at 1000-hPa level is chosen, as it is relevant to the frictional moisture convergence theory. Furthermore, low-level moisture flux divergence is dominated by the anomalous wind

divergence of the climatological specific humidity, while other terms in the moisture flux divergence equation are very small.

1) GENERAL ATMOSPHERIC CONDITION IN MAY–OCTOBER

The spatial structures associated with the EOF1 mode in May–October show large-scale low pressure anomalies over the western North Pacific and relatively high

EOF1 (Nov–Apr)
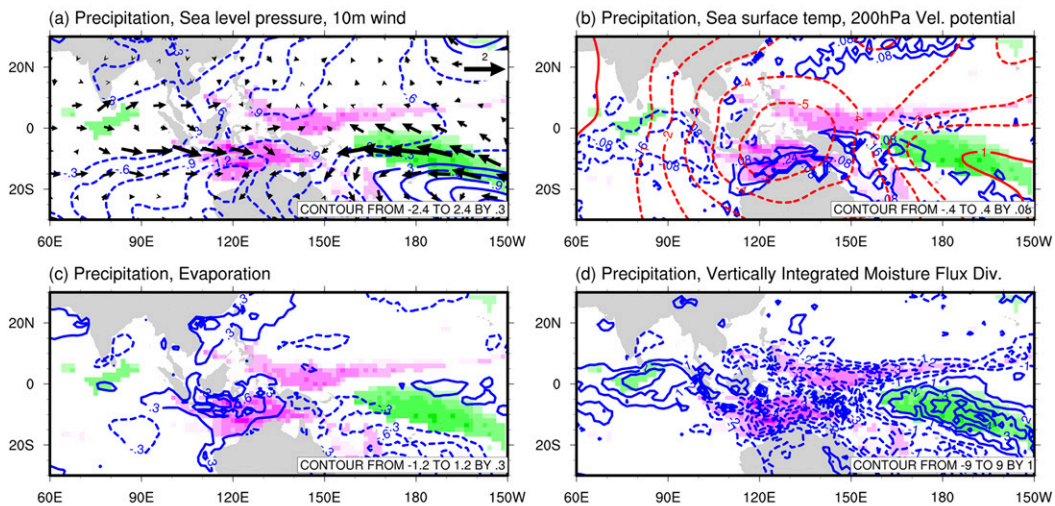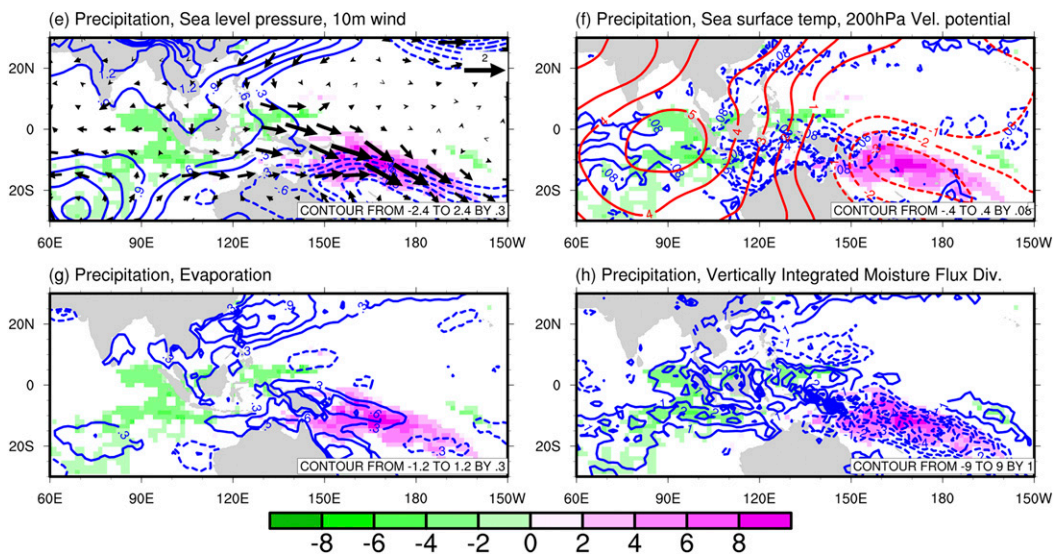

EOF2 (Nov–Apr)

FIG. 8. As in Fig. 7, but for November–April.

pressure anomalies over the Indian Ocean (Fig. 7a). Relatively strong westerly surface wind anomalies are found within and to the west of the active convection, while weaker easterly anomalies are found east of the convection. These anomalies mostly cause strengthened total wind to the east and west of the active convection, because the background winds in May–October are westerly over the Indian Ocean and easterly over the Pacific Ocean (Fig. S2). The enhanced surface evaporation within and west of the active convection (Fig. 7c) is consistent with the stronger wind. The surface evaporation also shows some positive anomalies to the north of the active convection over the South China Sea. Over

the same region, anomalous easterly flow and positive SST anomalies are also observed. The observed SST anomalies are a few tenths of a degree and of similar magnitude to those associated with intraseasonal variability (Hendon and Glick, 1997; Shinoda et al. 1998; Woolnough et al. 2000; Kemball-Cook and Wang, 2001; Cao et al. 2017). The 200-hPa velocity potential anomalies indicate that the rainfall anomalies are linked to deep convection and to a planetary-scale circulation pattern, in a structure consistent with the MJO (Fig. 7b). The vertically integrated moisture flux divergence and rainfall anomalies are in good agreement with each other (Fig. 7d).

For the EOF2 mode, the low pressure anomalies are shifted to the north of the equatorial region producing an anomalous cyclonic circulation centered around 20°N over the South China Sea (Fig. 7e). The wind anomalies are southwesterly within and to the southwest of the active convection and east-northeasterly to the north. Given the background wind (Fig. S2), this leads to stronger total wind speed in the region. Consistently, surface evaporation is also enhanced within and to the southwest and north of the active convection (Fig. 7g). As for the EOF1 mode, the positive rainfall anomalies and vertically integrated moisture flux convergence anomalies are in good agreement (Fig. 7h). The 200-hPa velocity potential anomalies over the western Pacific are weaker compared to that of the EOF1 mode. This is consistent with the weaker large-scale rainfall patterns (Fig. 7f) and with EOF2 representing the decay phase of this joint mode. The negative SST anomalies are collocated with the positive rainfall anomalies within and to the north of the active convection (Fig. 7f).

2) GENERAL ATMOSPHERIC CONDITION IN NOVEMBER–APRIL

The EOF1 mode in November–April shows enhanced rainfall over the Maritime Continent and suppressed rainfall over the SPCZ (Fig. 8a). Positive but weaker rainfall anomalies are also observed along the eastern coast of Australia (southwest of the SPCZ). Over the Maritime Continent, there are westerly wind anomalies within and to the west of the suppressed convection, while there are strong southeasterly wind anomalies in the South Pacific. The southeasterly wind anomalies along the SPCZ are associated with high pressure anomalies to the southwest of the mean SPCZ position, and relatively lower SLP anomalies over the Maritime Continent. The negative (positive) 200-hPa velocity potential anomalies over the Maritime Continent (South Pacific) indicate the presence of enhanced (suppressed) convection and are consistent with a planetary-scale mode of variability (Fig. 8b). The SST patterns associated with the EOF1 mode show warm SST anomalies to the south and southeast of the active convection that extends from the Maritime Continent to the South Pacific (Fig. 8b). While to the west of the active convection (i.e., over the Indian Ocean), negative SST anomalies are observed. Over the Maritime Continent, surface evaporation is enhanced (within and to the west of the active convection), whereas it is suppressed over the South Pacific (Fig. 8c). Interestingly, the negative evaporation anomalies are slightly southwest of the suppressed convection along the SPCZ. On the other hand, near the equatorial region to the northeast of the suppressed convection, positive evaporation anomalies

are observed. These positive evaporation anomalies are possibly caused by the easterly wind anomalies, as the climatological winds here are primarily from the east (Fig. S2c). The association between anomalous vertically integrated moisture flux divergence and rainfall is similar but less coherent than for the EOF modes in May–October (Fig. 8d).

In the case of the EOF2 mode, there is enhanced convection to the southeast of the mean SPCZ position and suppressed rainfall over the Maritime Continent and Indian Ocean (Fig. 8e). The enhanced convection in the South Pacific is characterized by negative SLP anomalies along the eastern coast of Australia and an anomalous cyclonic circulation. To the northeast of the anomalous cyclonic center, anomalous strong northwesterly flow is collocated with the positive rainfall anomalies. As for the EOF1 mode, the positive (negative) upper-level velocity potential anomalies over the Indian Ocean and Maritime Continent (South Pacific) indicate suppressed (enhanced) convection that is linked to a planetary-scale pattern of variability (Fig. 8f). There are negative SST anomalies to the east of the suppressed convection, and positive SST anomalies to the west of it (Fig. 8f). The negative SST anomalies are consistent with the increased surface evaporation (Fig. 8g) that is likely driven by the stronger northwesterly wind from Maritime Continent to the SPCZ. Furthermore, the vertically integrated moisture flux convergence (divergence) anomalies and positive (negative) rainfall anomalies are in good agreement with each other (Fig. 8h).

3) MECHANISMS FOR THE PROPAGATION OF RAINFALL

To better understand the time evolution of the 30–80-day rainfall variability and its relationship with atmospheric fields, we plot time–longitude and time–latitude rainfall anomalies (Fig. 9) and phase composites of area-averaged anomalous atmospheric fields (Fig. 10), using 30–80-day bandpass-filtered data. It is important to note that the longitudinal averaging in the time–latitude plots for both EOF modes in November–April are computed by defining a diagonal axis along the enhanced and shifted SPCZ positions, which correspond to the two EOF modes (Figs. 2c,d). The diagonal axis is constructed by identifying the latitudinal maximum rainfall anomaly along the enhanced and shifted SPCZ positions and fitting linear diagonal lines to these. Because the orientation and location of maximum loading along the SPCZ are different in the two EOF modes, the orientations of diagonal axes are also different. For each latitude, the average value is computed from 10°E to 10°W of the diagonal axis. Also, note that the time–longitude and
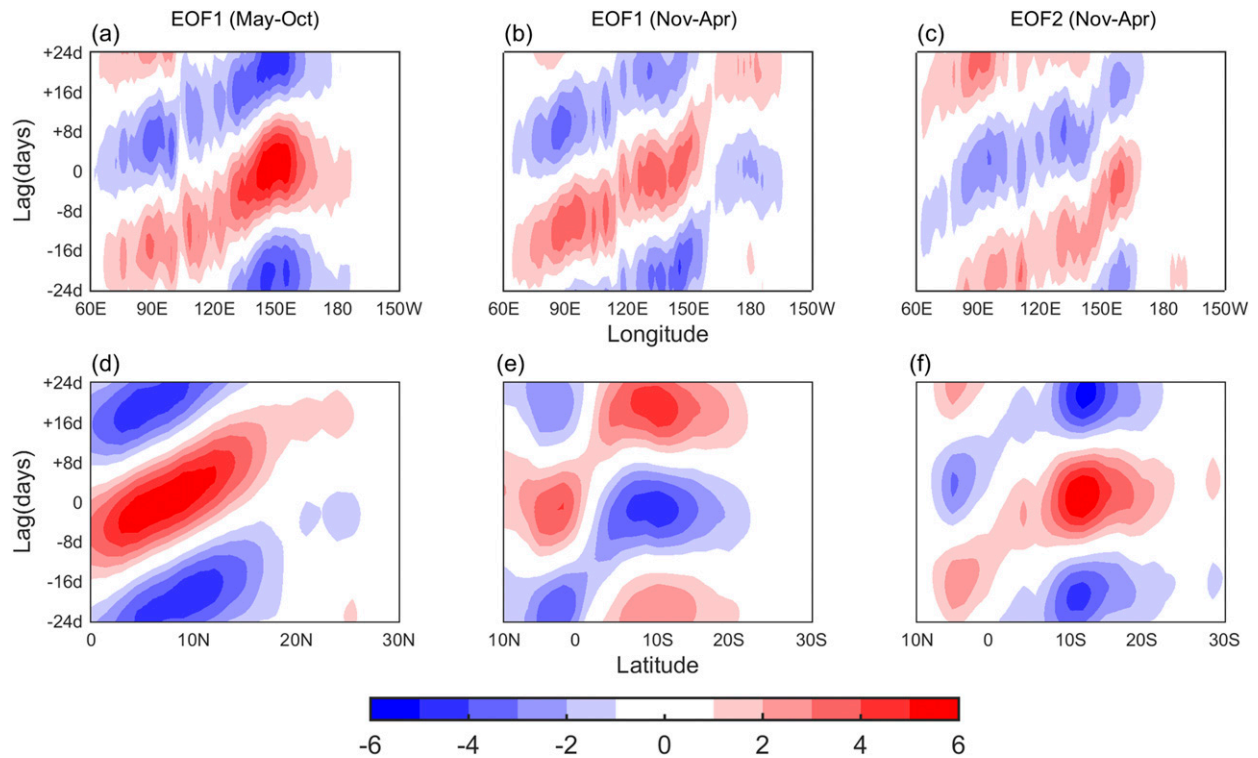
FIG. 9. (a)–(c) Time–longitude plot of 30–80-day rainfall anomalies (mm day^{-1}) averaged over 10°N to 5°S for May–October and 5°N to 10°S for November–April. (d)–(f) Time–latitude plot of rainfall anomalies averaged over 120°–150°E for May–October and along the diagonal rainfall axis over the South Pacific for November–April. In November–April, for both EOF modes, the diagonal axis is constructed by following the maximum rainfall variance along the enhanced and shifted SPCZ associated with each EOF mode. For each latitude, the region from 10°E and 10°W of the diagonal axis is selected for averaging. Only significant values at 95% confidence level are shown. Positive lags in days indicate the PC is leading.

time–latitude plots are only prepared for the EOF1 mode in May–October, because of the relatively high lag correlation between the two PCs.

The time–longitude and time–latitude plots of rainfall anomalies in May–October clearly show eastward propagation from 70° to 170°E and northward propagation from 0° to 15°N (Figs. 9a,d). The eastward propagation of rainfall anomalies is also present in both EOF modes in November–April with comparable magnitudes (Figs. 9b,c). However, the southeastward propagating rainfall signals (Figs. 9e,f) are less pronounced in November–April as compared to the northward propagation in May–October. Furthermore, the southeastward propagation of rainfall anomalies is mostly concentrated between 0°N and 10°S, while a relatively stationary signal is observed between 10° and 20°S.

The mechanisms governing the propagation of rainfall anomalies are identified by performing extensive phase composite and lag-correlation analysis to relate the PCs and the anomalous atmospheric fields. In particular, anomaly lag composites of primary atmospheric variables (SLP, SST, 1000-hPa moisture flux divergence,

evaporation, and wind speed at 10 m) and rainfall are computed (Figs. S3–S8). The results are synthesized in area-averaged anomaly lag composites. The area-averaged anomaly lag composites demonstrate the phase relationship among atmospheric fields and their connection with the rainfall anomalies along the region of propagation (Fig. 10). The composites are computed by taking weighted area averages of each field over six different regions (region A–G, Fig. 2). We selected these regions because the rainfall signals are pronounced in these locations and because the phase composites over these regions are easier to interpret, as maximum rainfall anomalies occur at zero lag. In May–October, the area-averaged time series is computed over an equatorial western Pacific (EWP) region and a northwestern Pacific (NWP) region. The EWP region (region A, Fig. 2) is selected to characterize the eastward propagation associated with the EOF1 mode and the NWP region (region B, Fig. 2) is selected to characterize the northward propagation associated with the EOF2 mode. For November–April, a Maritime Continent (MC) region and two South Pacific (SP) regions are selected.
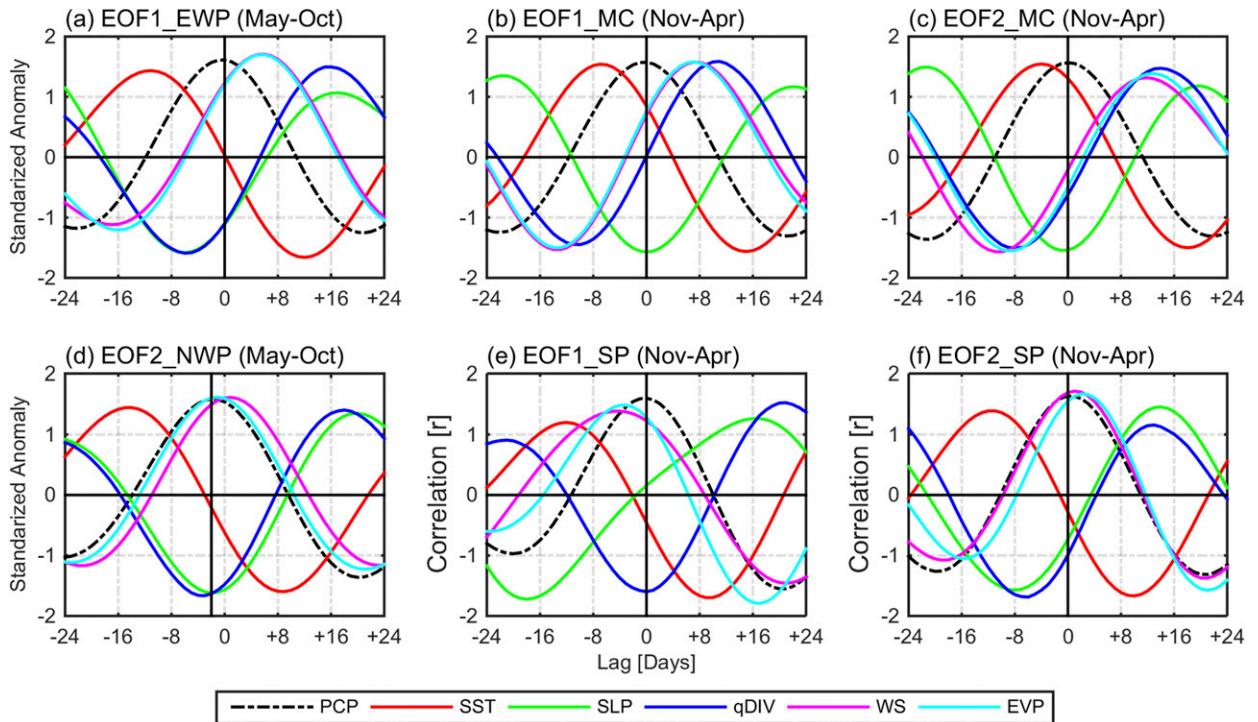
FIG. 10. Lag composites of 30–80-day anomalies of rainfall (PCP) (mm day^{-1}) and other atmospheric variables. The atmospheric variables used are SLP (mb), SST (°C), 10-m wind speed (WS) (m s^{-1}), evaporation (EVP) (mm day^{-1}), and 1000-hPa moisture flux divergence (qDIV) (10^{-6} g kg^{-1} s^{-1}). The fields are averaged over (a) equatorial western Pacific region 5°S–10°N, 130°–160°E (region A, Fig. 2a) for EOF1 mode in May–October; (b) Maritime Continent region 5°N–10°S, 110°–140°E (region C, Fig. 2c) for EOF1 mode in November–April; (c) Maritime Continent region 5°N–10°S, 110°–140°E (region E, Fig. 2d) for EOF2 mode in November–April; (d) northwestern Pacific region 5°–20°N, 120°–150°E (region B, Fig. 2b) for EOF2 mode in May–October; (e) South Pacific region 5°–15°S, 170°E–160°W (region D, Fig. 2c) for EOF1 mode in November–April; and (f) South Pacific region 5°–15°S, 150°E–180° (region F, Fig. 2d) for EOF2 mode in November–April. Positive lags in days indicate the PC is leading.

The MC region (region C and E, Fig. 2) is selected to characterize the eastward propagation. While the two SP regions (D and F, Fig. 2) are selected to characterize the different southeastward propagation in the two EOF modes. For comparison, the area-averaged fields are standardized by their respective time standard deviations. The top row in Fig. 10 represents the eastward propagation of rainfall and the bottom row represents the northward in May–October and southeastward propagation in November–April.

The phase composite approach used here assumes that the rainfall signal is propagating. It can provide insight on the propagation mechanisms when the composite is based on an index of rainfall averaged over a region in the path of the propagating rainfall signal (e.g., Hendon and Glick 1997; Tseng et al. 2015). In this case, the development phase of the composite also corresponds to what occurs ahead of the propagating signal, while the decay phase of the composite corresponds to what occurs to the rear of the propagating signal. Thus, the time axis can be considered as the distance along the path of propagation. The sensitivity of the results to the

selected boxes was checked by considering different boxes shifted along the propagation pathway. Shifting the location of the boxes along the propagation pathway by 5°–15° results in comparable relations between anomalies of rainfall and other atmospheric variables. This provides confidence in the propagation mechanisms. Note that the low-level moisture flux divergence anomalies presented in this section refer to the horizontal moisture flux divergence anomalies at 1000-hPa level.

The phase relationship between anomalies of rainfall and atmospheric fields for the eastward propagating rainfall signal in both seasons shows warm SST, low SLP and low-level moisture convergence leading the rainfall pattern. The maximum rainfall anomalies are then followed by positive wind speed and evaporation anomalies. Though the eastward propagating rainfall patterns in both May–October and November–April have a similar mechanism, the phase relationship between anomalies of rainfall and atmospheric fields are a little different. The time lag between SST and rainfall anomalies is 12 days (SST leading rainfall) in May–October, while in November–April anomalies of SST lead

rainfall by seven and five days for the EOF1 and EOF2 modes, respectively. Furthermore, the negative SLP anomalies and positive rainfall anomalies are maximum at zero lag in November–April for both EOF modes; however, SLP anomalies tend to lead rainfall anomalies in May–October. The eastward propagation of rainfall anomalies does not appear to be driven by wind speed caused changes in evaporation, as positive anomalies of evaporation and wind speed do not lead the active convection for the EOF modes in both seasons; but they may partly contribute to precondition the next suppressed phase, by producing cold SST anomalies to the east of the suppressed convection. Thus, low-level moisture flux convergence appears to be the most relevant mechanism for the eastward propagation of rainfall anomalies in both seasons.

To better understand the role of low-level moisture flux divergence, composites of moisture flux divergence from the surface to the upper troposphere are computed by taking the weighted area average over the same six regions (Fig. 11). Remember that the horizontal moisture flux divergence presented here is dominated by the anomalous wind divergence of climatological specific humidity. Consistent with Fig. 10, the near-surface moisture flux convergence anomalies lead the positive rainfall anomalies by 6–10 days and becomes deeper (up to 500 hPa) when the positive rainfall anomalies are maximum at lag zero (Figs. 11a–c). As the propagation is eastward, this corresponds to a westward tilt of moisture flux convergence anomalies. Thus, low-level moisture flux convergence ahead of the active convection appears to help precondition the deep convection. A similar frictional low-level moisture flux convergence mechanism has also been suggested by Tseng et al. (2015), and our results are comparable with their findings.

Though the underlying mechanisms for the eastward propagation of rainfall anomalies in both seasons for both EOF modes are fairly similar, the mechanisms for northward propagation in May–October and southeastward propagation in November–April show some noticeable differences (Figs. 10d–f). The northward propagation of rainfall anomalies associated with the joint EOF mode in May–October shows positive SST anomalies and low-level moisture flux convergence leading the active convective phase. The time lags are different compared to that for the eastward propagation, in particular, anomalous low-level moisture convergence only slightly leads anomalous rainfall. The vertical structure of moisture flux divergence anomalies is also different; it is mainly limited to below 850 hPa and shows little evidence of tilting (Fig. 11d). In addition, positive anomalies of surface wind speed and evaporation are almost in phase with the positive rainfall anomalies

(Fig. 10d). This relation indicates that wind speed anomalies may drive anomalous evaporation and contribute to the northward propagation of rainfall anomalies in May–October. The dominant impact of wind speed on the evaporation over the tropical Ocean has been documented by previous studies (Krishnamurti et al. 1988; Hendon and Glick 1997; DeMott et al. 2014) and our results are consistent with these. Thus, both low-level moisture flux convergence and evaporation could contribute to the northward propagation of the EOF1 and EOF2 related rainfall anomalies in May–October; and the relation among anomalies of SST, wind speed, evaporation, and rainfall indicates a mechanism similar to the wind–evaporation–SST feedback (Emanuel 1987; Neelin et al. 1987; Wang 1988; Xie and Philander 1994; Zhang 1996; Xie and Carton 2004; Lin et al. 2008).

The phase relation among anomalies of southeastward propagating rainfall and atmospheric fields are different for the two EOF modes in November–April (Figs. 10e,f). For the EOF1 mode, positive evaporation and wind speed anomalies lead the active convection by three to four days, and low-level moisture flux convergence anomalies are in phase with positive rainfall anomalies. In contrast, for the EOF2 mode, low-level moisture flux convergence anomalies lead positive rainfall anomalies by seven days, but both wind speed and evaporation anomalies are in phase with the rainfall anomalies. Furthermore, the SLP anomalies lead the rainfall anomalies, being almost in phase with the moisture flux divergence anomalies. In the case of the EOF1 mode, the SLP anomalies lead the rainfall anomalies by around 18 days, and thus their relationship is not clear. Interestingly, the phase relationship between anomalies of rainfall and SST are fairly similar in both the EOF modes, with positive SST anomalies leading positive rainfall anomalies. The relation among SST, wind speed, evaporation, and rainfall anomalies for EOF1 mode is reminiscent of the wind–evaporation–SST feedback; and there is little evidence of vertical tilting in moisture flux divergence for this mode over the South Pacific (Fig. 11e). While in case of EOF2 mode, low-level moisture flux convergence anomalies appear to be important for the development of convection over the South Pacific, and this is supported by the vertical tilting in moisture flux convergence anomalies (Fig. 11f).

5. Summary and discussion

The daily TRMM rainfall data has been used to investigate the 10–90-day patterns of variability in the western Pacific. Two leading EOF modes are identified in the May–October and November–April climatological periods. The spatial structures of 10–90-day
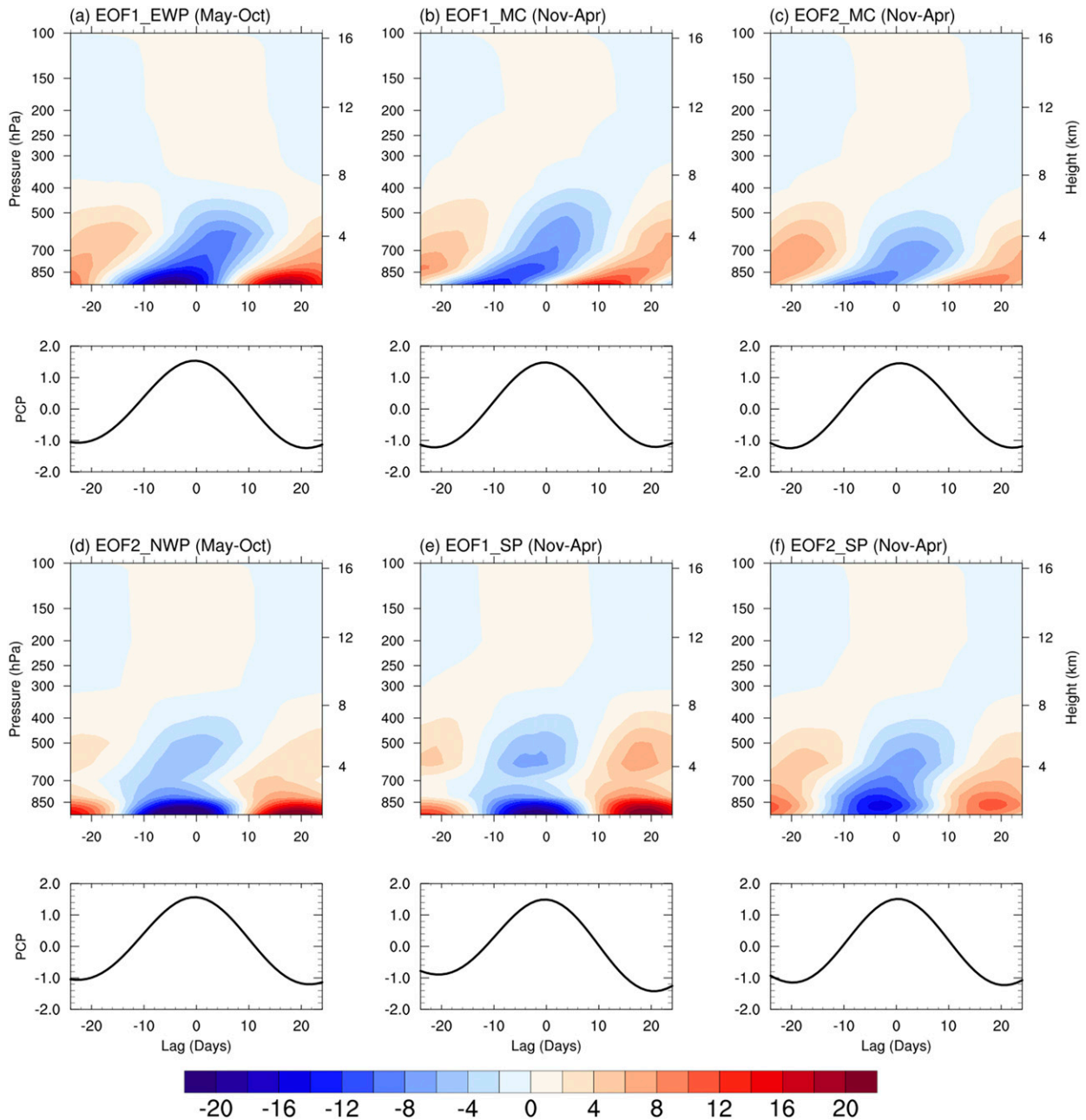
FIG. 11. Lag composites of the 30–80-day moisture flux divergence (10^{-6} g kg^{-1} s^{-1}) from the surface to the upper troposphere based on the standardized PCs (shaded). Negative values indicate convergence. The moisture flux divergence is averaged over the same six regions as described in Fig. 10. The line plots are corresponding composites of standardized rainfall anomalies (mm day^{-1}) averaged over the same regions.

EOF modes in May–October closely resemble one of the phases of Monsoon intraseasonal oscillation investigated in previous studies (Krishnamurthy and Shukla 2008; Suhas et al. 2013; Lee et al. 2013; Shukla 2014). Similarly, the spatial structures associated with the suppressed and shifted SPCZ modes in November–April are fairly similar to the EOF modes obtained by Matthews (2012).

The 30–80-day variability associated with the two EOF modes in both climatological periods are related to the MJO. The two EOF modes correspond to MJO phases 5 and 6 in May–October and MJO phases 4 and 6 in November–April. In May–October, the two EOFs are associated with eastward and northward propagation of rainfall anomalies that resemble the typical MJO propagation patterns (Lawrence and Webster 2002; Wheeler

and Hendon 2004; Chou and Hsueh 2010). In addition, the two PCs exhibit a relatively high lag-correlation and the MJO explains a large part of their variability. Thus, the leading EOF modes in May–October appear to be a manifestation of two different phases of the MJO.

In November–April, the two EOFs are associated with eastward propagation of rainfall anomalies resembling the MJO, but southeastward propagation over the South Pacific is less distinct. In addition, the lag-correlation between the two PCs is weak and the MJO explains relatively little variance in two PCs. Thus, in November–April, the two EOF modes appear to be independently associated with the MJO, and are less influenced by the MJO compared to in May–October; this is despite that the MJO signal is overall more pronounced in December–March (Zhang and Dong 2004). The lesser relative importance of the MJO over the South Pacific in November–April is consistent with the lower MJO explained variance during these months as compared to May–October (Figs. 1c,d). Furthermore, the difference in propagation mechanisms for the two EOF modes in November–April could explain why the two modes appear to be influenced by different MJO events. Scale interactions among the MJO, ENSO, and the SPCZ (Hendon et al. 2007; Tang and Yu 2008; Matthews 2012) may explain why the two EOF modes appear to be independently influenced by the MJO. Understanding such interactions is an interesting topic for a future study.

The eastward propagation of 30–80-day rainfall variability associated with the two EOF modes in both seasons is characterized by the low-level moisture flux convergence mechanism, with a potential positive SST feedback. The mechanism is consistent with the low-level moisture convergence mechanism proposed for the propagation of MJO (Wang and Rui 1990; Hendon and Salby 1994; Maloney and Hartmann 1998; Matthews 2000; Sperber 2003; Lin et al. 2004; Yang et al. 2008; Tseng et al. 2015). In particular, we show that anomalously warm SST and low-level moisture flux convergence anomalies develop ahead of the active convection, where at the same time there are negative wind speed and evaporation anomalies. The positive SST anomalies to the east of the increased rainfall could enhance the moist static energy by increasing the surface equivalent potential temperature and thereby destabilize the atmospheric column east of the active convection (Flatau et al. 1997; Hendon and Glick 1997; Lau and Sui 1997; Tseng et al. 2015). On the other hand, the warm SST anomalies could also lower the surface pressure, supporting moisture flux convergence in advance of the convection (Wang and Xie 1998; Waliser et al. 1999; Kemball-Cook et al. 2002; Maloney and Kiehl 2002). The enhancement of wind speed and evaporation a few days after the passage of active convection and the cooling tendency of SST suggests that the evaporation is primarily controlled by the development of westerly wind anomalies.

Low-level moisture flux convergence and wind–evaporation–SST feedback appear to drive the northward propagation of 30–80-day rainfall anomalies associated with the two EOF modes in May–October. However, low-level moisture flux convergence anomalies only slightly lead anomalous deep convection in the northward propagation, and the vertical profile of anomalous moisture flux divergence is very shallow (limited to 850 hPa and below). The SST here seems to be primarily driven by wind speed and evaporation, and warm (cold) SST anomalies appear to drive low (high) sea level pressure anomalies. On the one hand, low sea level pressure anomalies could support frictional low-level moisture flux convergence. On the other hand, they could also enhance the evaporation by supporting easterly and northeasterly wind anomalies. Cao et al. (2017) document similar northward propagation of SST anomalies over the western North Pacific and the South China Sea in May–October.

Different mechanisms govern the southeastward propagation of 30–80-day rainfall anomalies in November–April over the South Pacific associated with two leading modes. For the EOF1 mode, the wind–evaporation–SST feedback appears to be a relevant mechanism for the propagation, whereas, for the EOF2 mode, low-level moisture flux convergence seems to be important. The mechanism driving southeastward propagation of rainfall anomalies associated with the EOF1 mode in November–April appears similar to that driving northward propagation in the May–October, except that the wind speed and evaporation anomalies now lead instead of slightly lag the rainfall anomalies. Increase in wind speed to the southeast of the convection could potentially enhance surface evaporation, and thereby help to destabilize the atmosphere and supply moisture to higher levels supporting the southeastward propagation. Unlike the EOF1 mode, the development of the low-level moisture flux convergence southeast of the active convection seems to contribute to the southeastward propagation of rainfall anomalies associated with the EOF2 mode in November–April. The essential role of moisture flux divergence in the case of the EOF2 mode is also supported by the tilted vertical profile of anomalous moisture flux divergence over the South Pacific. However, the maximum moisture flux divergence anomalies are not at the surface as in the other cases. Here, the maximum moisture divergence anomalies are observed at 850-hPa level. It is not clear why this is the case and it needs further study.

An interesting feature associated with the 30–80-day rainfall variability in November–April is the link between rainfall anomalies over the South Pacific and the circulation anomalies over the South China Sea (Figs. 7 and 8). A statistically significant signal of strong northerly flow from the South China Sea to the South Pacific is evident in the phase composites at zero lag for both EOF modes (Figs. 8a,e), but the signal is more pronounced in the EOF2 mode. Consistent with the wind anomalies, the surface evaporation anomalies are also positive over the South China Sea (Figs. 8c,g). Such strengthening of the circulation over the South China Sea and associated positive evaporation feedback, particularly in the case of the EOF2 mode, may interact with the eastward propagating MJO signal over the Maritime Continent (Chang et al. 2005; Chang et al. 2016), and consequently modulate the rainfall variability over the South Pacific. Hence, understanding of such interaction and its implication to the 30–80-day rainfall variability over the South Pacific could be useful to explain the discrepancy in the propagation mechanisms for two EOF modes in November–April.

In summary, the investigation of intraseasonal rainfall variability and its relation to the MJO presented here helps to explain the key characteristics of the dominant rainfall patterns, with their eastward and northward propagation in May–October and their eastward and southeastward propagation in November–April. Based on previous studies along with results presented here, we suggest that the low-level moisture flux divergence and the wind–evaporation–SST feedback mechanism are relevant for the intraseasonal rainfall variability over the western Pacific. However, the different propagation mechanisms for two dominant EOF modes in November–April and their linear relation with MJO suggests dynamically different relations with the MJO. Numerical experiments would be helpful to better understand such discrepancy in the mechanisms and the connection to the MJO.

REFERENCES

Bain, C. L., J. De Paz, J. Kramer, G. Magnusdottir, P. Smyth, H. Stern, and C. C. Wang, 2011: Detecting the ITCZ in instantaneous satellite data using spatiotemporal statistical modeling: ITCZ climatology in the east Pacific. *J. Climate*, **24**, 216–230, https://doi.org/10.1175/2010JCLI3716.1.

Biello, J. A., and A. J. Majda, 2005: A new multiscale model for the Madden–Julian oscillation. *J. Atmos. Sci.*, **62**, 1694–1721, https://doi.org/10.1175/JAS3455.1.

Bladé, I., and D. L. Hartmann, 1993: Tropical intraseasonal oscillations in a simple nonlinear model. *J. Atmos. Sci.*, **50**, 2922–2939, https://doi.org/10.1175/1520-0469(1993)050<2922:TIOIAS>2.0.CO;2.

Borlace, S., A. Santoso, W. Cai, and M. Collins, 2014: Extreme swings of the South Pacific convergence zone and the different types of El Niño events. *Geophys. Res. Lett.*, **41**, 4695–4703, https://doi.org/10.1002/2014GL060551.

Bretherton, C. S., P. N. Blossey, and M. Khairoutdinov, 2005: An energy-balance analysis of deep convective self-aggregation above uniform SST. *J. Atmos. Sci.*, **62**, 4273–4292, https://doi.org/10.1175/JAS3614.1.

Cao, X., R. Wu, and S. Chen, 2017: Contrast of 10–20-day and 30–60-day intraseasonal SST propagation during summer and winter over the South China Sea and western North Pacific. *Climate Dyn.*, **48**, 1233–1248, https://doi.org/10.1007/s00382-016-3138-z.

Chang, C. P., P. A. Harr, and H. J. Chen, 2005: Synoptic disturbances over the equatorial South China Sea and western Maritime Continent during boreal winter. *Mon. Wea. Rev.*, **133**, 489–503, https://doi.org/10.1175/MWR-2868.1.

——, M. M. Lu, and H. Lim, 2016: Monsoon convection in the Maritime Continent: Interaction of large-scale motion and complex terrain. *Multiscale Convection-Coupled Systems in the Tropics: A Tribute to Dr. Michio Yania*, Meteor. Monogr., No. 56, Amer. Meteor. Soc., 6.1–6.29, https://doi.org/10.1175/AMSMONOGRAPHS-D-15-0011.1.

Chen, T. C., and M. Murakami, 1988: The 30–50 day variation of convective activity over the western Pacific Ocean with emphasis on the northwestern region. *Mon. Wea. Rev.*, **116**, 892–906, https://doi.org/10.1175/1520-0493(1988)116<0892:TDVOCA>2.0.CO;2.

——, M. C. Yen, and S. P. Weng, 2000: Interaction between the summer monsoons in East Asia and the South China Sea: Intraseasonal monsoon modes. *J. Atmos. Sci.*, **57**, 1373–1392, https://doi.org/10.1175/1520-0469(2000)057<1373:IBTSMI>2.0.CO;2.

Chou, C., and Y. C. Hsueh, 2010: Mechanisms of northward-propagating intraseasonal oscillation—A comparison between the Indian Ocean and the western North Pacific. *J. Climate*, **23**, 6624–6640, https://doi.org/10.1175/2010JCLI3596.1.

Dee, D. P., and Coauthors, 2011: The ERA-Interim reanalysis: Configuration and performance of the data assimilation system. *Quart. J. Roy. Meteor. Soc.*, **137**, 553–597, https://doi.org/10.1002/qj.828.

DeMott, C. A., C. Stan, D. A. Randall, and M. D. Branson, 2014: Intraseasonal variability in coupled GCMs: The roles of ocean feedbacks and model physics. *J. Climate*, **27**, 4970–4995, https://doi.org/10.1175/JCLI-D-13-00760.1.

——, N. P. Klingaman, and S. J. Woolnough, 2015: Atmosphere-ocean coupled processes in the Madden–Julian oscillation.

Rev. Geophys., **53**, 1099–1154, https://doi.org/10.1002/2014RG000478.

Ding, Y., 1992: Summer monsoon rainfalls in China. *J. Meteor. Soc. Japan*, **70**, 373–396, https://doi.org/10.2151/jmsj1965.70.1B_373.

Dommenget, D., 2007: Evaluating EOF modes against a stochastic null hypothesis. *Climate Dyn.*, **28**, 517–531, https://doi.org/10.1007/s00382-006-0195-8.

Emanuel, K. A., 1987: An air-sea interaction model of intraseasonal oscillations in the tropics. *J. Atmos. Sci.*, **44**, 2324–2340, https://doi.org/10.1175/1520-0469(1987)044<2324:AASIMO>2.0.CO;2.

Falkland, A., 2002: Tropical island hydrology and water resources: Current knowledge and future needs. *Hydrology and Water Resources Management in the Humid Tropics, Proc. Second Int. Colloquium*, UNESCO-IHP-V Tech. Doc. in Hydrology Tech. Doc. 52, Panama, Republic of Panama, UNESCO, 237–298.

——, and E. Custodio, 1991: Hydrology and water resources of small islands: A practical guide. Unesco Rep. 49, 435 pp.

Feldstein, S. B., 2000: The timescale, power spectra, and climate noise properties of teleconnection patterns. *J. Climate*, **13**, 4430–4440, https://doi.org/10.1175/1520-0442(2000)013<4430:TTPSAC>2.0.CO;2.

Flatau, M., P. J. Flatau, P. Phoebus, and P. P. Niiler, 1997: The feedback between equatorial convection and local radiative and evaporative processes: The implications for intra-seasonal oscillations. *J. Atmos. Sci.*, **54**, 2373–2386, https://doi.org/10.1175/1520-0469(1997)054<2373:TFBECA>2.0.CO;2.

Folland, C. K., J. A. Renwick, M. J. Salinger, and A. B. Mullan, 2002: Relative influences of the interdecadal Pacific oscillation and ENSO on the South Pacific convergence zone. *Geophys. Res. Lett.*, **29**, 1643, https://doi.org/10.1029/2001GL014201.

Gawander, J., 2007: Impact of climate change on sugar-cane production in Fiji. *WMO Bull.*, **56**, 34–39.

Gilman, D. L., F. J. Fuglister, and J. M. Mitchell Jr., 1963: On the power spectrum of "red noise." *J. Atmos. Sci.*, **20**, 182–184, https://doi.org/10.1175/1520-0469(1963)020<0182:OTPSON>2.0.CO;2.

Haffke, C., and G. Magnusdottir, 2013: The South Pacific convergence zone in three decades of satellite images. *J. Geophys. Res. Atmos.*, **118**, 10 839–10 849, https://doi.org/10.1002/jgrd.50838.

Harrison, D. E., and N. K. Larkin, 1998: El Niño-Southern Oscillation sea surface temperature and wind anomalies, 1946–1993. *Rev. Geophys.*, **36**, 353–399, https://doi.org/10.1029/98RG00715.

Hendon, H. H., and M. L. Salby, 1994: The life cycle of the Madden–Julian oscillation. *J. Atmos. Sci.*, **51**, 2225–2237, https://doi.org/10.1175/1520-0469(1994)051<2225:TLCOTM>2.0.CO;2.

——, and J. Glick, 1997: Intra-seasonal air-sea interaction in the tropical Indian and Pacific Oceans. *J. Climate*, **10**, 647–661, https://doi.org/10.1175/1520-0442(1997)010<0647:IASIIT>2.0.CO;2.

——, M. Wheeler, and C. Zhang, 2007: Seasonal dependence of the MJO–ENSO relationship. *J. Climate*, **20**, 531–543, https://doi.org/10.1175/JCLI4003.1.

Hsu, H. H., and M. Y. Lee, 2005: Topographic effects on the eastward propagation and initiation of the Madden–Julian oscillation. *J. Climate*, **18**, 795–809, https://doi.org/10.1175/JCLI-3292.1.

Huffman, G. J., and Coauthors, 2007: The TRMM Multisatellite Precipitation Analysis (TMPA): Quasi-global, multiyear, combined-sensor precipitation estimates at fine scales. *J. Hydrometeor.*, **8**, 38–55, https://doi.org/10.1175/JHM560.1.

Kang, I. S., C. H. Ho, Y. K. Lim, and K. M. Lau, 1999: Principal modes of climatological seasonal and intra-seasonal variations of the Asian summer monsoon. *Mon. Wea. Rev.*, **127**, 322–340, https://doi.org/10.1175/1520-0493(1999)127<0322:PMOCSA>2.0.CO;2.

Kemball-Cook, S., and B. Wang, 2001: Equatorial waves and air–sea interaction in the boreal summer intraseasonal oscillation. *J. Climate*, **14**, 2923–2942, https://doi.org/10.1175/1520-0442(2001)014<2923:EWAASI>2.0.CO;2.

——, and B. C. Weare, 2001: The onset of convection in the Madden–Julian oscillation. *J. Climate*, **14**, 780–793, https://doi.org/10.1175/1520-0442(2001)014<0780:TOOCIT>2.0.CO;2.

——, B. Wang, and X. Fu, 2002: Simulation of the intra-seasonal oscillation in the ECHAM-4 model: The impact of coupling with an ocean model. *J. Atmos. Sci.*, **59**, 1433–1453, https://doi.org/10.1175/1520-0469(2002)059<1433:SOTIOI>2.0.CO;2.

Knutson, T. R., and K. M. Weickmann, 1987: 30–60 day atmospheric oscillations: Composite life cycles of convection and circulation anomalies. *Mon. Wea. Rev.*, **115**, 1407–1436, https://doi.org/10.1175/1520-0493(1987)115<1407:DAOCLC>2.0.CO;2.

Krishnamurthy, V., and J. Shukla, 2008: Seasonal persistence and propagation of intra-seasonal patterns over the Indian monsoon region. *Climate Dyn.*, **30**, 353–369, https://doi.org/10.1007/s00382-007-0300-7.

Krishnamurti, T. N., D. K. Oosterhof, and A. V. Mehta, 1988: Air–sea interaction on the timescale of 30 to 50 days. *J. Atmos. Sci.*, **45**, 1304–1322, https://doi.org/10.1175/1520-0469(1988)045<1304:AIOTTS>2.0.CO;2.

Lau, K. M., and P. H. Chan, 1986: Aspects of the 40–50 day oscillation during the northern summer as inferred from outgoing longwave radiation. *Mon. Wea. Rev.*, **114**, 1354–1367, https://doi.org/10.1175/1520-0493(1986)114<1354:AOTDOD>2.0.CO;2.

——, and L. Peng, 1987: Origin of low-frequency (intraseasonal) oscillations in the tropical atmosphere. Part I: Basic theory. *J. Atmos. Sci.*, **44**, 950–972, https://doi.org/10.1175/1520-0469(1987)044<0950:OOLFOI>2.0.CO;2.

——, and C. H. Sui, 1997: Mechanisms of short-term sea surface temperature regulation: Observations during TOGA COARE. *J. Climate*, **10**, 465–472, https://doi.org/10.1175/1520-0442(1997)010<0465:MOSTSS>2.0.CO;2.

——, G. J. Yang, and S. H. Shen, 1988: Seasonal and intraseasonal climatology of summer monsoon rainfall over Eeat Asia. *Mon. Wea. Rev.*, **116**, 18–37, https://doi.org/10.1175/1520-0493(1988)116<0018:SAICOS>2.0.CO;2.

——, L. Peng, T. Nakazawa, and C. H. Sui, 1989: Dynamics of super cloud clusters, westerly wind bursts, 30–60 day oscillations and ENSO—A unified view. *J. Meteor. Soc. Japan*, **67**, 205–219, https://doi.org/10.2151/jmsj1965.67.2_205.

Lawrence, D. M., and P. J. Webster, 2002: The boreal summer intraseasonal oscillation: Relationship between northward and eastward movement of convection. *J. Atmos. Sci.*, **59**, 1593–1606, https://doi.org/10.1175/1520-0469(2002)059<1593:TBSIOR>2.0.CO;2.

Lee, J. Y., B. Wang, M. C. Wheeler, X. Fu, D. E. Waliser, and I. S. Kang, 2013: Real-time multivariate indices for the boreal summer intra-seasonal oscillation over the Asian summer monsoon region. *Climate Dyn.*, **40**, 493–509, https://doi.org/10.1007/s00382-012-1544-4.

Li, T., and B. Wang, 2005: A review on the western North Pacific monsoon: Synoptic-to-interannual variabilities. *Terr. Atmos. Oceanic Sci.*, **16**, 285–314, https://doi.org/10.3319/TAO.2005.16.2.285(A).

Lin, J., B. Mapes, M. Zhang, and M. Newman, 2004: Stratiform precipitation, vertical heating profiles, and the Madden–Julian oscillation. *J. Atmos. Sci.*, **61**, 296–309, https://doi.org/10.1175/1520-0469(2004)061<0296:SPVHPA>2.0.CO;2.

——, W. Han, and X. Lin, 2008: Observational analysis of the wind–evaporation–SST feedback over the tropical Pacific Ocean. *Atmos. Sci. Lett.*, **9**, 231–236, https://doi.org/10.1002/asl.195.

Lindzen, R. S., 1974: Wave-CISK and tropical spectra. *J. Atmos. Sci.*, **31**, 1447–1449, https://doi.org/10.1175/1520-0469(1974)031<1447:WCATS>2.0.CO;2.

Madden, R. A., and P. R. Julian, 1994: Observations of the 40–50-day tropical oscillation—A review. *Mon. Wea. Rev.*, **122**, 814–837, https://doi.org/10.1175/1520-0493(1994)122<0814:OOTDTO>2.0.CO;2.

Majda, A. J., and R. Klein, 2003: Systematic multiscale models for the tropics. *J. Atmos. Sci.*, **60**, 393–408, https://doi.org/10.1175/1520-0469(2003)060<0393:SMMFTT>2.0.CO;2.

——, and J. A. Biello, 2004: A multiscale model for tropical intraseasonal oscillations. *Proc. Natl. Acad. Sci. USA*, **101**, 4736–4741, https://doi.org/10.1073/pnas.0401034101.

——, and S. N. Stechmann, 2009: A simple dynamical model with features of convective momentum transport. *J. Atmos. Sci.*, **66**, 373–392, https://doi.org/10.1175/2008JAS2805.1.

Maloney, E. D., and D. L. Hartmann, 1998: Frictional moisture convergence in a composite life cycle of the Madden–Julian oscillation. *J. Climate*, **11**, 2387–2403, https://doi.org/10.1175/1520-0442(1998)011<2387:FMCIAC>2.0.CO;2.

——, and J. T. Kiehl, 2002: MJO-related SST variations over the tropical eastern Pacific during Northern Hemisphere summer. *J. Climate*, **15**, 675–689, https://doi.org/10.1175/1520-0442(2002)015<0675:MRSVOT>2.0.CO;2.

Matthews, A. J., 2000: Propagation mechanisms for the Madden-Julian oscillation. *Quart. J. Roy. Meteor. Soc.*, **126**, 2637–2651, https://doi.org/10.1002/qj.49712656902.

——, 2012: A multiscale framework for the origin and variability of the South Pacific Convergence Zone. *Quart. J. Roy. Meteor. Soc.*, **138**, 1165–1178, https://doi.org/10.1002/qj.1870.

——, and H. Y. Y. Li, 2005: Modulation of station rainfall over the western Pacific by the Madden-Julian oscillation. *Geophys. Res. Lett.*, **32**, L14827, https://doi.org/10.1029/2005GL023595.

McPhaden, J. M., X. Zhang, H. Henden, and C. Wheeler, 2006: Large scale dynamics and MJO forcing of ENSO variability. *Geophys. Res. Lett.*, **33**, LI6702, https://doi.org/10.1029/2006GL026786.

Murakami, T., 1980: Empirical orthogonal function analysis of satellite-observed outgoing longwave radiation during summer. *Mon. Wea. Rev.*, **108**, 205–222, https://doi.org/10.1175/1520-0493(1980)108<0205:EOFAOS>2.0.CO;2.

Nakazawa, T., 1992: Seasonal phase lock of intra-seasonal variation during the Asian summer monsoon. *J. Meteor. Soc. Japan*, **70**, 597–611.

Neelin, J. D., I. M. Held, and K. H. Cook, 1987: Evaporation–wind feedback and low-frequency variability in the tropical atmosphere. *J. Atmos. Sci.*, **44**, 2341–2348, https://doi.org/10.1175/1520-0469(1987)044<2341:EWFALF>2.0.CO;2.

North, G. R., T. L. Bell, R. F. Cahalan, and F. J. Moeng, 1982: Sampling errors in the estimation of empirical orthogonal functions. *Mon. Wea. Rev.*, **110**, 699–706, https://doi.org/10.1175/1520-0493(1982)110<0699:SEITEO>2.0.CO;2.

Raymond, D. J., and Ž. Fuchs, 2009: Moisture modes and the Madden–Julian oscillation. *J. Climate*, **22**, 3031–3046, https://doi.org/10.1175/2008JCLI2739.1.

Rui, H., and B. Wang, 1990: Development characteristics and dynamic structure of tropical intraseasonal convection anomalies. *J. Atmos. Sci.*, **47**, 357–379, https://doi.org/10.1175/1520-0469(1990)047<0357:DCADSO>2.0.CO;2.

Shinoda, T., H. H. Hendon, and J. Glick, 1998: Intraseasonal variability of surface fluxes and sea surface temperature in the tropical western Pacific and Indian Oceans. *J. Climate*, **11**, 1685–1702, https://doi.org/10.1175/1520-0442(1998)011<1685:IVOSFA>2.0.CO;2.

Shukla, R. P., 2014: The dominant intraseasonal mode of intra-seasonal South Asian summer monsoon. *J. Geophys. Res. Atmos.*, **119**, 635–651, https://doi.org/10.1002/2013JD020335.

Sperber, K. R., 2003: Propagation and the vertical structure of the Madden–Julian oscillation. *Mon. Wea. Rev.*, **131**, 3018–3037, https://doi.org/10.1175/1520-0493(2003)131<3018:PATVSO>2.0.CO;2.

Suhas, E., J. M. Neena, and B. N. Goswami, 2013: An Indian monsoon intraseasonal oscillations (MISO) index for real time monitoring and forecast verification. *Climate Dyn.*, **40**, 2605–2616, https://doi.org/10.1007/s00382-012-1462-5.

Tanaka, M., 1992: Intra-seasonal oscillation and the onset and retreat dates of the summer monsoon over east, southeast Asia and the western Pacific region using GMS high cloud amount data. *J. Meteor. Soc. Japan*, **70**, 613–629.

Tang, Y., and B. Yu, 2008: MJO and its relationship to ENSO. *J. Geophys. Res.*, **113**, D14106, https://doi.org/10.1029/2007JD009230.

Torrence, C., and G. P. Compo, 1998: A practical guide to wavelet analysis. *Bull. Amer. Meteor. Soc.*, **79**, 61–78, https://doi.org/10.1175/1520-0477(1998)079<0061:APGTWA>2.0.CO;2.

Tseng, W. L., B. J. Tsuang, N. S. Keenlyside, H. H. Hsu, and C. Y. Tu, 2015: Resolving the upper-ocean warm layer improves the simulation of the Madden–Julian oscillation. *Climate Dyn.*, **44**, 1487–1503, https://doi.org/10.1007/s00382-014-2315-1.

——, H. H. Hsu, N. Keenlyside, C. W. June Chang, B. J. Tsuang, C. Y. Tu, and L. C. Jiang, 2017: Effects of surface orography and land–sea contrast on the Madden–Julian oscillation in the Maritime Continent: A numerical study using ECHAM5-SIT. *J. Climate*, **30**, 9725–9741, https://doi.org/10.1175/JCLI-D-17-0051.1.

Van Der Wiel, K., A. J. Matthews, D. P. Stevens, and M. M. Joshi, 2015: A dynamical framework for the origin of the diagonal South Pacific and South Atlantic convergence zones. *Quart. J. Roy. Meteor. Soc.*, **141**, 1997–2010, https://doi.org/10.1002/qj.2508.

Waliser, D. E., K. M. Lau, and J. H. Kim, 1999: The influence of coupled sea surface temperatures on the Madden–Julian oscillation: A model perturbation experiment. *J. Atmos. Sci.*, **56**, 333–358, https://doi.org/10.1175/1520-0469(1999)056<0333:TIOCSS>2.0.CO;2.

Wang, B., 1988: Dynamics of tropical low-frequency waves: An analysis of the moist Kelvin wave. *J. Atmos. Sci.*, **45**, 2051–2065, https://doi.org/10.1175/1520-0469(1988)045<2051:DOTLFW>2.0.CO;2.

——, and H. Rui, 1990: Dynamics of the coupled moist Kelvin–Rossby wave on an equatorial β-plane. *J. Atmos. Sci.*, **47**, 397–413, https://doi.org/10.1175/1520-0469(1990)047<0397:DOTCMK>2.0.CO;2.

——, and X. Xu, 1997: Northern Hemisphere summer monsoon singularities and climatological intraseasonal oscillation. *J. Climate*, **10**, 1071–1085, https://doi.org/10.1175/1520-0442(1997)010<1071:NHSMSA>2.0.CO;2.

——, and X. Xie, 1998: Coupled modes of the warm pool climate system. Part I: The role of air–sea interaction in maintaining Madden–Julian oscillation. *J. Climate*, **11**, 2116–2135, https://doi.org/10.1175/1520-0442-11.8.2116.

——, F. Huang, Z. Wu, J. Yang, X. Fu, and K. Kikuchi, 2009: Multiscale climate variability of the South China Sea monsoon: A review. *Dyn. Atmos. Oceans*, **47**, 15–37, https://doi.org/10.1016/j.dynatmoce.2008.09.004.

Wheeler, M. C., and H. H. Hendon, 2004: An all-season real-time multivariate MJO index: Development of an index for monitoring

and prediction. *Mon. Wea. Rev.*, **132**, 1917–1932, https://doi.org/10.1175/1520-0493(2004)132<1917:AARMMI>2.0.CO;2.

White, I., T. Falkland, and D. Scott, 1999: Droughts in small coral islands: Case study, South Tarawa, Kiribati. IHP-V Tech. Doc. in Hydrology, Tech. Doc. 26, Unesco, 55 pp.

Woolnough, S. J., J. M. Slingo, and B. J. Hoskins, 2000: The relationship between convection and sea surface temperature on intraseasonal timescales. *J. Climate*, **13**, 2086–2104, https://doi.org/10.1175/1520-0442(2000)013<2086:TRBCAS>2.0.CO;2.

Wu, R., and B. Wang, 2001: Multi-stage onset of the summer monsoon over the western North Pacific. *Climate Dyn.*, **17**, 277–289, https://doi.org/10.1007/s003820000118.

Xie, S. P., and A. Kubokawa, 1990: On the wave-CISK in the presence of a frictional boundary layer. *J. Meteor. Soc. Japan*, **68**, 651–657, https://doi.org/10.2151/jmsj1965.68.6_651.

——, and S. G. H. Philander, 1994: A coupled ocean-atmosphere model of relevance to the ITCZ in the eastern Pacific. *Tellus*, **46A**, 340–350, https://doi.org/10.3402/tellusa.v46i4.15484.

——, and J. A. Carton, 2004: Tropical Atlantic variability: Patterns, mechanisms, and impacts. *Earth Climate: The Ocean-Atmosphere Interaction*, *Geophys. Monogr.*, Vol. 147, Amer. Geophys. Union, 121–142, https://doi.org/10.1029/147GM07.

Yamasaki, M., 1969: Large-scale disturbances in the conditionally unstable atmosphere in low latitudes. *Pap. Meteor. Geophys.*, **20**, 289–336, https://doi.org/10.2467/mripapers1950.20.4_289.

Yang, B., X. Fu, and B. Wang, 2008: Atmosphere-ocean conditions jointly guide convection of the boreal summer intra-seasonal oscillation: Satellite observations. *J. Geophys. Res.*, **113**, D11105, https://doi.org/10.1029/2007JD009276.

Zhang, C., 1996: Atmospheric intraseasonal variability at the surface in the tropical western Pacific Ocean. *J. Atmos. Sci.*, **53**, 739–758, https://doi.org/10.1175/1520-0469(1996)053<0739:AIVATS>2.0.CO;2.

——, 2005: Madden–Julian Oscillation. *Rev. Geophys.*, **43**, RG2003, https://doi:10.1029/2004RG000158.

——, 2013: Madden–Julian oscillation: Bridging weather and climate. *Bull. Amer. Meteor. Soc.*, **94**, 1849–1870, https://doi.org/10.1175/BAMS-D-12-00026.1.

——, and M. Dong, 2004: Seasonality in the Madden–Julian oscillation. *J. Climate*, **17**, 3169–3180, https://doi.org/10.1175/1520-0442(2004)017<3169:SITMO>2.0.CO;2.